# Locally tuned deformation fields combination for 2D cine-MRI-based driving of 3D motion models

*D. Dasnoy-Sumell[1], A. Aspeel[1], K. Souris[2], B. Macq[1]*

[1] D. Dasnoy-Sumell (damien.dasnoy@uclouvain.be),
A. Aspeel (antoine.aspeel@uclouvain.be) and
B. Macq (benoit.macq@uclouvain.be)
are with the Universite Catholique de Louvain, Institute of Information and Communication Technologies, Electronics and Applied Mathematics, ImagX-R lab, Place du Levant 3 Box L5.03.02, 1348 Louvain-la-Neuve, Belgium

Damien Dasnoy-Sumell and A. Aspeel are supported by the Walloon Region, SPWEER Win2Wal program project 2010149

[2] K. Souris (kevin.souris@uclouvain.be) is with the Universite Catholique de Louvain, Institut de Recherche Experimentale et Clinique (IREC), Molecular Imaging, Radiotherapy and Oncology (MIRO), Avenue Hippocrate 54 Box B1.54.07, 1200 Brussels, Belgium

Kevin Souris is funded by the Walloon region (MECATECH/BIOWIN, grant number 8090)

Corresponding author: Damien Dasnoy-Sumell (damien.dasnoy@uclouvain.be)

Conflict of interest:
Kevin Souris is involved in a research collaboration with IBA s.a. and is funded by the Walloon Region (Belgium)

## Abstract

Purpose: To target mobile tumors in radiotherapy with the recent MR-Linac hardware solutions, research is being conducted to drive a 3D motion model with 2D cine-MRI to reproduce the breathing motion in 4D. This work presents a method to combine several deformation fields using local measures to better drive 3D motion models.
Methods: The method uses weight maps, each representing the proximity with a specific area of interest. The breathing state is evaluated on cine-MRI frames in these areas and a different deformation field is estimated for each using a 2D to 3D motion model. The different deformation fields are multiplied by their respective weight maps and combined to form the final field to apply to a reference image. A global motion model is adjusted locally on the selected areas and creates a 3DCT for each cine-MRI frame.
Results: The 13 patients on which it was tested showed on average an improvement of the accuracy of our model of 0.71 mm for areas selected to drive the model and 0.5 mm for other areas compared to our previous method without local adjustment. The additional computation time for each region was around 40 ms on a modern laptop.
Conclusion: The method improves the accuracy of the 2D-based driving of 3D motion models. It can be used on top of existing methods relying on deformation fields. It does add some computation time but, depending on the area to deform and the number of regions of interests, offers the potential of online use.

Keywords: 3D motion model, Cine-MRI, IGRT, Real-time tracking, Image processing

# 1. Introduction

Targeting abdominal or lung tumors with radio- or proton therapy is not an easy task. The respiratory motion that occurs during the treatment, as well as more irregular motions such as bladder filling or systematic shifts in the patient anatomy, must be considered in planning treatments to be as accurate and robust as possible. Methods exist to mitigate the motion amplitude [1] or regularize the breathing pattern [2]. Margins are commonly used to ensure target coverage [3], and sometimes robust optimization [4, 5].

In recent years, MRI and radiotherapy have been combined in hybrid machines capable of delivering photon treatments and taking MR images simultaneously [6]. MRI presents better soft-tissue contrast than CT scans with the added advantage that no imaging dose is given to the patient. For now, MRI is not fast enough to acquire time-resolved 3D images at sufficient frequency to follow the breathing pattern of a patient continuously; only 2D acquisitions are available at those frequencies. Research is currently aimed at driving a 3D patient-specific motion model using 2D cine-MRI to reproduce the breathing pattern of a patient in 4D continuously for an entire treatment fraction.

Among the different methods that have been developed to achieve this, some use the combination, interpolation, or extrapolation of precomputed deformation fields between the 3D images (usually called phases) of a planning 4DMRI or 4DCT [7]. The resulting field is then applied to a reference image to create the 3D anatomy of a specific time point. One may use a principal component analysis-based motion model [8], [9] in which a global metric is computed using the entire slice or navigators extracted from the 2D slice [10]. The motion occurring out of plane can be quantified using a priori information on planning data [11]. And our previous work using fast border tracking and an averaging over several local information from the 2D slice to strive for use in real time [12]. For these methods, the deformation applied to the reference image in order to get the 3D image matching the current 2D frame is applied globally, without local adjustments using local information. The issue is that if non-breathing related motion occurs between the acquisition of the motion model data and the treatment, the motion model might not contain the deformation necessary to reproduce the patient's current anatomy. To reduce this issue, methods using local information exist. A region-of-interest (ROI)-based model [13] has been derived from Fayad et al. [10] and used to split the deformation fields into regions for each ROI. It improves the precision of the reproduced motion but takes too much time to use online.

**Contributions**

We propose an additional step to tune these deformation field-based global methods using local information, one that lets us create images that are adjusted locally by combining several deformation fields, each created specifically for a certain area of the image. These areas can be chosen, for example, to improve the model's guidance in the beam path and around the target. We applied this additional step on our previous work, the border tracking-based method [12], because it focuses on speed and online use and to compare easily the complete process with and without this step. We also analyzed the results in function of the chosen area of interests, to try to extract guidelines for the use of such motion models. In our case the breathing state is measured locally using tissue border trackers, but the combination of deformation fields presented here could also be used with other 3D motion model methods as long as the chosen method can be applied piecewise to different image areas to produce deformation fields. The resulting fields for each area can then be combined using the method we propose here to improve the accuracy of the model by adjusting the result on the chosen areas [Figure 1].

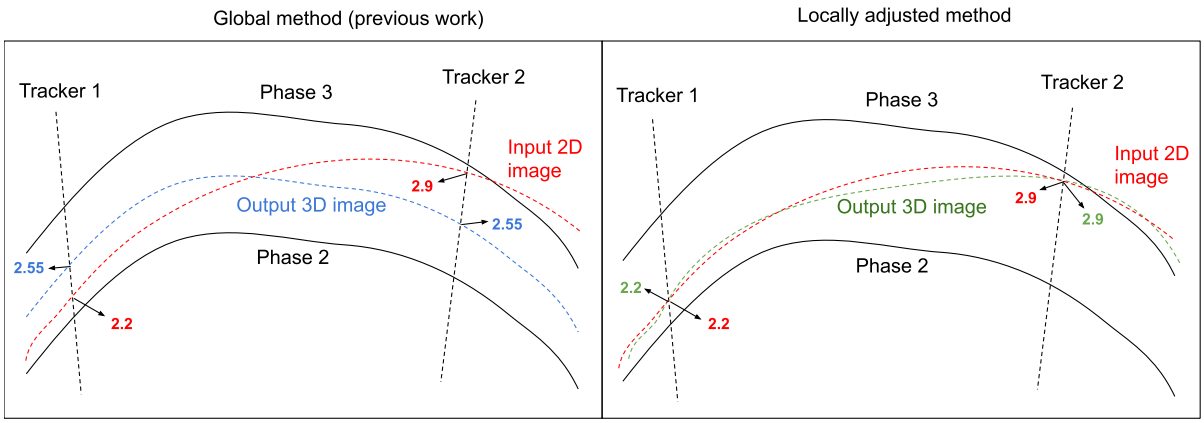


Figure 1: Schematic example of our method with (right) and without (left) the local tuning of the deformation fields. An organ border is represented in two different positions, respectively the positions on the phases 2 and 3 of a planning 4D image (black lines). On the left the global method without the local tuning. The breathing state is evaluated relatively to the planning 4DCT using two border trackers (dotted black lines). The trackers evaluate the position of the border in the input image that we want to reproduce (red dotted line) as 2.2 and 2.9 respectively, relatively to the phases 2 and 3 of the planning 4DCT. The output of the motion model is a 3D image, created by deformation of a reference image, in which the position of the tracked border is at the average of these two measures, in this example an interpolated phase 2.55 in blue dotted line. On the right the same situation with the same input 2D image but with our proposed local tuning. The output 3D image is this time the green dotted line, adjusted on the two tracker areas to match the positions 2.2 and 2.9.

## 2. Materials and Methods

The method is divided into two parts. First the preparation step, itself split into offline preparation to build the motion model and online preparation to register the cine-MRI on the model 4DCT images and to choose the important areas to adjust the deformation. Then the second part is the online application once the preparation is done, which takes a stream of cine-MRI 2D frames and gives a 3DCT for each, potentially in real time (see discussions). The method is summarized in Figure 2, then each step is described hereunder.

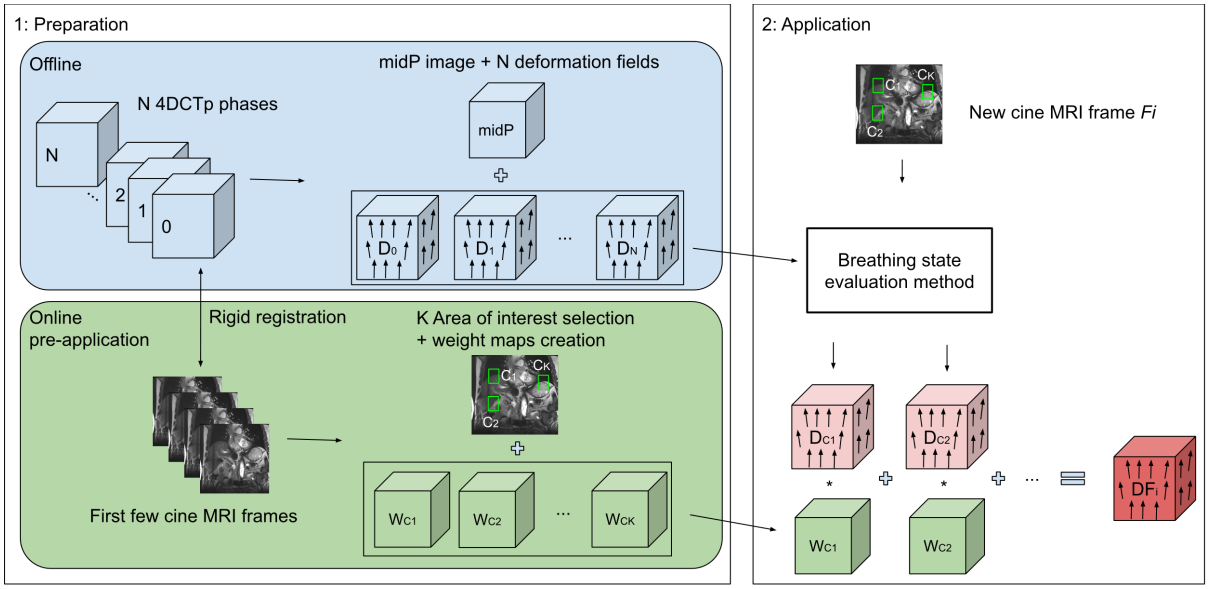


Figure 2. Schematic representation of the method. On the left the preparation step, where first the planning 4DCT (4DCTp) is used to compute a midP image and deformation fields from this midP image to each of the 4DCTp phases. After that the first few images of the cine-MRI acquisition are first registered on the 4DCTp and then used to choose areas of interest to drive the model. A 3D weight map is then computed for each of those areas. On the right the application step once the preparation is done. A new cine-MRI frame is given to a breathing state evaluation method, which measures the breathing state in the areas of interest and returns a 3D deformation field associated with each area. Finally, the different 3D deformation fields are used in combination with the weight maps to create the final deformation field $DF_i$ to apply to the midP image.

## 2.1 Preparation

The motion model creation is similar to our previous work [12] but using less deformation fields. Prior to continuous application, a planning 4DCT (4DCTp) of N=10 phases was acquired. From this 4DCTp, non-rigid registration Morphons' algorithm $[14]$ was used to compute *N*-1 deformation fields from the first phase to each of the other phases. The mid-position image (midP) image is created by computing the average of all these *N*-1 deformation fields, then by deforming all phases on the average position and taking the median value for each voxel $[15]$. The midP image and the $N$ 3D deformation fields $D_n(x, y, z)$ from the midP image to each of the $N$ 4DCTp phases was stored and formed the motion model from which the images would be derived. Compared to our previous work we do not use the fields from a phase to the next, but only the fields from the midP image to each of the $N$ 4DCTp phases.

Once the 2D cine-MRI sequence is launched, but before starting to generate the 3D images using the motion model, MRI 2D plane positions must be registered on the 4DCTp. This work was done manually in this study using vertebrae, since we had a limited number of patients, but could be automated using multi-modal rigid registration algorithms. This way, a 2D position on the MRI images can be transferred in 3D to the 4DCTp.

## 2.2 Area selection and weight map creation

Then, the areas in which the breathing state would be evaluated were selected. This was a set of $K$ points $C_k = (x_k, y_k, z_k)$ that were the centers of areas in which the breathing state would be measured, and the motion model adjusted locally. As the goal here was to evaluate the impact of motion on the dose delivered during a radiotherapy treatment fraction with cine-MRI images

available, the interesting areas were selected on 2D cine-MRI slices. As MRI is very flexible in terms of image orientation and position, it is always possible to acquire a slice passing through the target and in the beam path. In practice, the way the regions and points $C_k$ are defined depends on the breathing state evaluation method [Section 2.3]. For this part we used a small set of three to five manually placed border trackers $T_k$ as in our previous work [12], where tissue interfaces were chosen as regions of interest and the area center $C_k$ was the center of the tracker $T_k$. Using these trackers, the motion is measured in one dimension in the tracker direction, which can be oblique and does not have to align with one of the anatomical axis (left-right, cranio-caudal, antero-posterior). The chosen tissue borders must be visible on both cine-MR and 4DCTp images, preferably perpendicular to their motion and with a large range of motion. Good candidates are the hepatic dome, left diaphragmatic dome, visceral liver surface, kidneys, skin, etc. Liver tumors are usually not visible on cine-MRI or 4DCTp images or both, so it was not possible to use the tumors consistently as a tracker position. The same regions were selected automatically on both the 2D MRI sequence and the 4DCTp thanks to the registration [Figure 3].

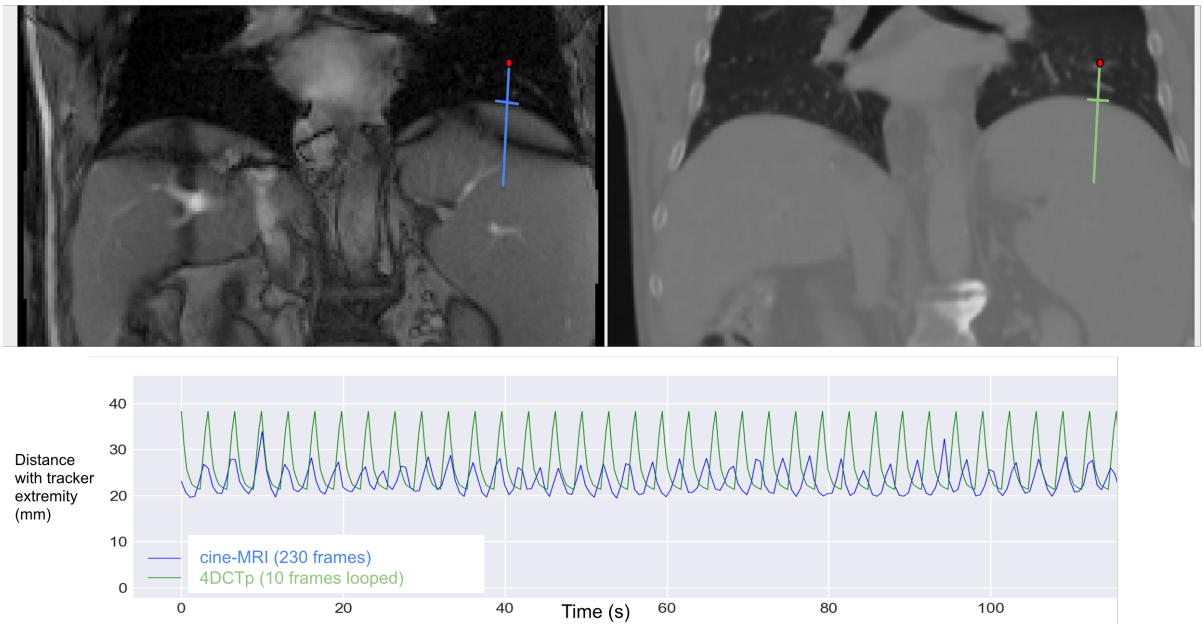


Figure 3. Example of area selection by placing a tracker on the left diaphragmatic dome for a cine-MRI sequence (left) and the corresponding slice of the 4DCTp (right). The resulting motion signals are given as the distance between the tracker's extremity (red dot) which corresponds to 0 in the graph and the tracked border (small perpendicular line). We can see that the motion of the diaphragm at this position was around 20 mm in the 4DCTp, but when the patient came for the cine-MRI acquisition its breathing was less deep, and the motion was slightly under 10 mm.

The last thing to do in the preparation step was to create the weight maps, which were 3D maps of the same size as the 4DCTp images. Selected areas' centers $C_k = (x_k, y_k, z_k)$ were derived from each of the $K$ areas and used to compute the $K$ 3D piecewise linear weight maps $W_k(x, y, z)$ according to the following steps, depicted in Figure 4.

1. Create an empty matrix of the size of the 3D images.
2. Set the voxel at position $C_k$ to 1 and the voxels at all other positions $C_{j \neq k}$ to 0.
3. Add points at the 8 corners of a twice-as-big matrix centered on the 3D image and give them the value 1/*K*.
4. Fill the rest of the matrix by piecewise linear interpolation.

These weight maps $W_k$ form a Lagrange interpolation basis and represent a proximity map for each voxel of the image with the position $C_k$, shielded by the other positions $C_{j\neq k}$ and converging to 1/$K$ for voxels far from all the $K$ trackers.

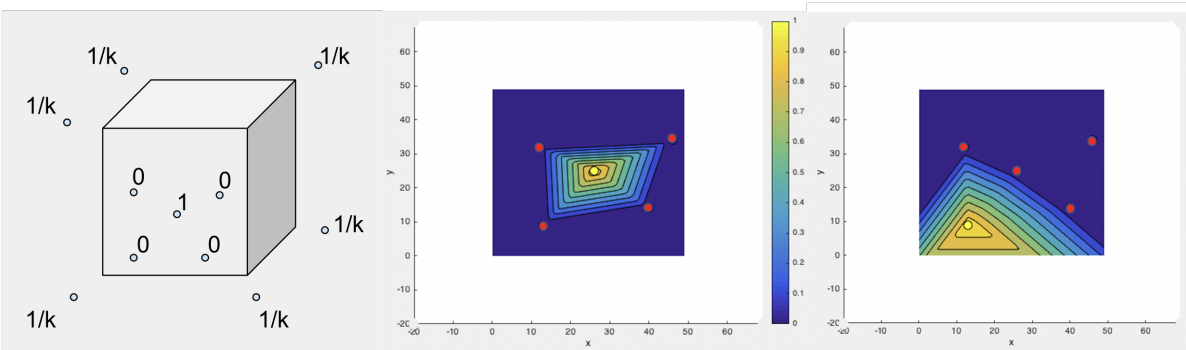


Figure 4. 3D schematic example of weight map preparation (left). The position $C_k$ is set to 1, the other tracker positions $C_{j\neq k}$ are set to 0, and the eight corners of a larger cube outside the image are set to 1/$K$ ($K$=5 in this example). The weight map is then filled by piecewise linear interpolation. The center and right images show resulting slices extracted from two different resulting 3D weight maps after filling by interpolation. This shows how the values in the weight maps go from 1 on the position $C_k$ to 0 to the positions $C_{j\neq k}$. The positions $C_{j\neq k}$ act like some sort of shields to block the impact of the position $C_k$ for areas of the weight map located behind them. The points $C_{j\neq k}$ are shown in red for visibility but have the value 0.

To apply our method to another motion model method, such as the ones cited in the introduction, the area selection method might differ, but the weight maps would be created the same way.

### 2.3 Breathing state evaluation

The breathing state at a given time is quantified locally relatively to the motion reference of the planning 4DCT. Our metric would, for instance, provide a value of 2.4 for a breathing state measured at 40% of the distance between Phase 2 and Phase 3 of the 4DCTp. This is done using the tracker method described in our previous work [12] and summarized here after. The same border position is measured in one dimension in the tracker direction for the midP image, for the 10 images of the 4DCTp and for the current MRI frame $F_i$. The relative distances between the measured position for the frame $F_i$ and the other images are used to compute an inter-or extrapolation ratio and determine the breathing state for this frame $F_i$ at the position of this tracker [Figure 5]. If the border position on the MRI frame is measured inside the range of the 4DCTp, the breathing state will be an interpolation between the two surrounding phases (Like the 2.4 breathing state example we gave previously). If the measured $F_i$ position is outside the range of the 4DCTp, we call this an extrapolation case and the breathing state is computed using the distance between the border position in the midP image and in the extremum phase, compared with the distance between the position in the midP image and in the frame $F_i$ [Figure 5]. This is done for each tracker $T_k$ independently, such as different breathing states can be detected for different areas of the anatomy. For example, for a given frame Fi of the cine-MRI, a tracker T1 on the hepatic dome can measure a 2.4 breathing state where another tracker T2 on the left diaphragmatic dome can measure a 1.8 breathing state.

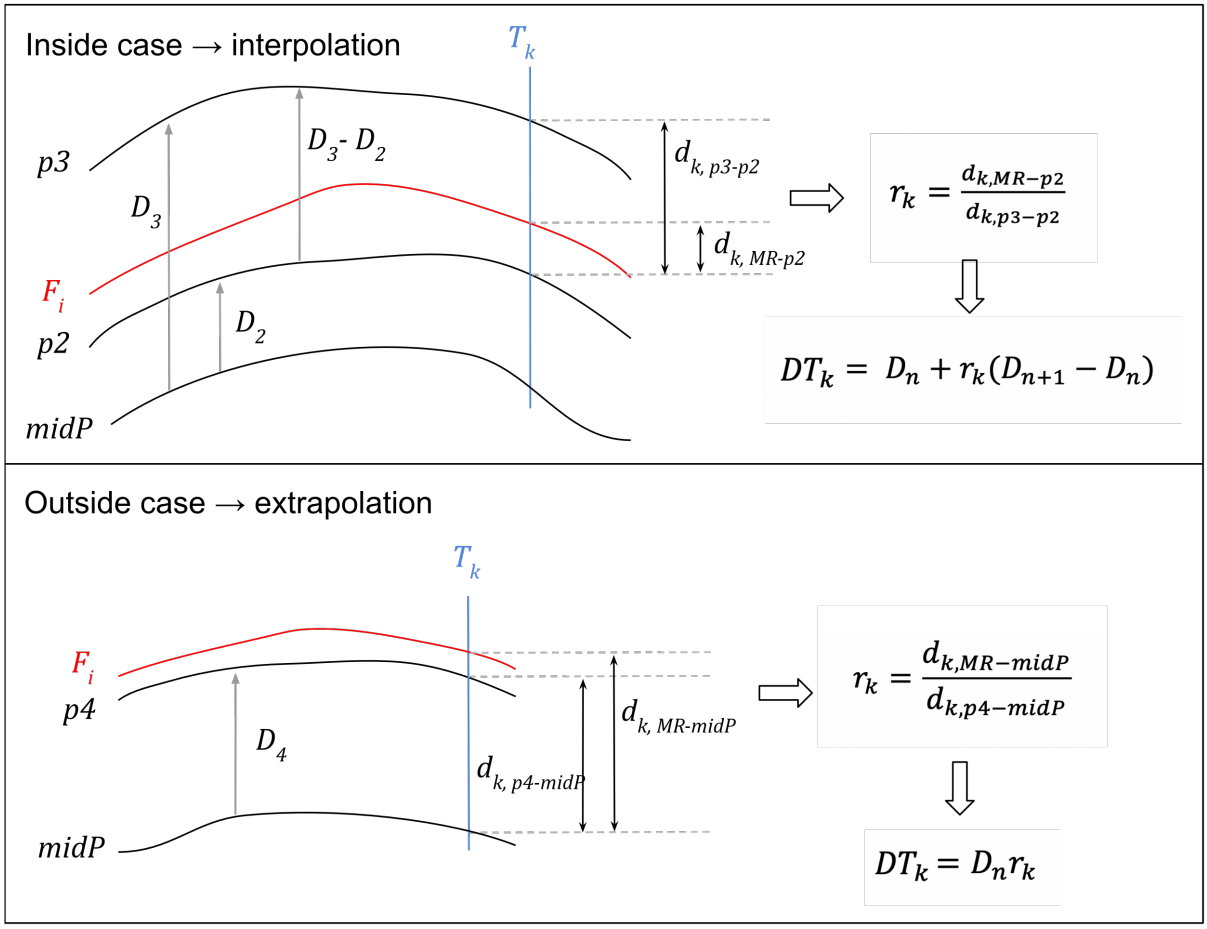


Figure 5. For each tracker $T_k$, the position of the MR frame $F_i$ is compared with the positions of the other phases $pN$ and the midP image in this tracker. The ratio $r_k$ is computed with the position differences $d_k$ measured in the tracker $T_k$. There are two possible cases, namely, interpolation, when the $F_i$ position is inside the range of the 4DCTp phases (top), and extrapolation, when the $F_i$ position is outside the range of the 4DCTp phases (bottom). The ratio $r_k$ is then used in combination with the deformation fields of the motion model to compute the field $DT_k$. The field $DT_k$ is the field that, applied to the reference midP image, allows to create the $3DCT_i$ image for the frame $F_i$ in which the border tracked by the tracker $T_k$ is at the same position as in the frame $F_i$.

### 2.4 3D image deformation

Then, a 3D deformation field $DT_k$ is computed for the tracker $T_k$ using a combination of fields from the motion model fields $D_n$ and a ratio $r_k$ based on the tracked border position in this tracker. This can be done in two different ways, depending on whether the tracked border is inside or outside the range of positions represented in the motion model [Figure 5]. Compared to our previous work [12], we only use fields from the midP image to the other phases and not from a phase to the following one. Note that the deformation field $DT_k$ depends on the current frame $F_i$ but the dependency in $i$ is omitted for the sake of conciseness. The field $DT_k$ is the field that is locally adjusted to the measured breathing state at the position of the tracker $T_k$. If applied to the midP image, it would give a 3DCT image in which the border position is the same as in the MRI frame. But as we do this for multiple trackers, an additional step is necessary to combine the fields $DT_k$ created for each tracker.

Each field $DT_k$ is multiplied by the weight map $W_k$ and summed to create the final field $DF_i$ to apply to the midP image for the frame $F_i$. It gives a field that is locally equivalent to each of the $DT_k$ fields on their corresponding trackers' positions $C_k$ and interpolated in-between. Formally it is

$$DF_i(x,y,z) = \sum_k DT_k(x,y,z)W_k(x,y,z),$$

which implies

$$DF_i(x_k,y_k,z_k) = DT_k(x_k,y_k,z_k).$$

Formally, our method receives deformation fields associated with points in the image volume $\{(C_k, D_k)\}_{k=1,\dots,K}$ and returns a unique interpolated deformation field $DF_i$. For each 2D frame $F_i$, the created field $DF_i$ is used to deform the midP image to a $3DCT_i$ and complete the continuous 4DCT (4DCTc). This new 4DCTc image sequence follows the breathing pattern of the cine-MRI over the entire 2 minutes of the image sequence. It is not just one breathing period like the 4DCTp.

## 2.5 Materials

The data came from thirteen patients treated for liver tumours by radiotherapy. MR images are True FISP sequences [16] (Siemens Skyra 3T) of two interleaved slices (coronal and sagittal planes), acquired for two minutes in treatment position with abdominal compression and centered on the tumor (Example in Figure 9). The acquisition of both planes took 550 ms, which makes an acquisition frequency of 3.63 images per second because each frame is used independently. Every slice, coronal or sagittal, is used to create a 3DCT corresponding to the slice time point, that result in around 440 3DCT images for each patient. Images are 192 x 188 pixels wide with 1.82 mm/pixel in both directions. A 4DCT was also acquired the same day under the same conditions. This trial was carried out in accordance with the World Medical Association's Code of Ethics (Declaration of Helsinki) for experiments involving humans and approved by our local ethics committee (B403201628906).

## 2.6 Validation

To determine whether the method could reproduce the MRI motion, which was the ground truth, we first observed the difference between each frame $F_i$ and the resulting $3DCT_i$. The average of the absolute values of the differences between tracked border positions for each $F_i - 3DCT_i$ pair over the entire cine-MRI sequence was computed for each tracker and gives what we call the tracker's result. This was done for two types of ROI, i.e., the areas already used to drive the model (DT for Driving Trackers) and new areas where trackers were placed for validation purposes (VT for Validation Trackers). In these new areas that were not used to create the image, the local breathing state was interpolated by the weighted sum of the deformation fields. Figure 6 shows an example where we can see that it was possible to reproduce the motion of the MRI at different tracker positions quite well, even if there were slight changes compared with the original motion model (in this case the patient's breathing amplitude is lower than when the 4DCTp was acquired) and if the patient breathes outside the range of the planning 4DCTp (with a baseline shift, for example, [17]).

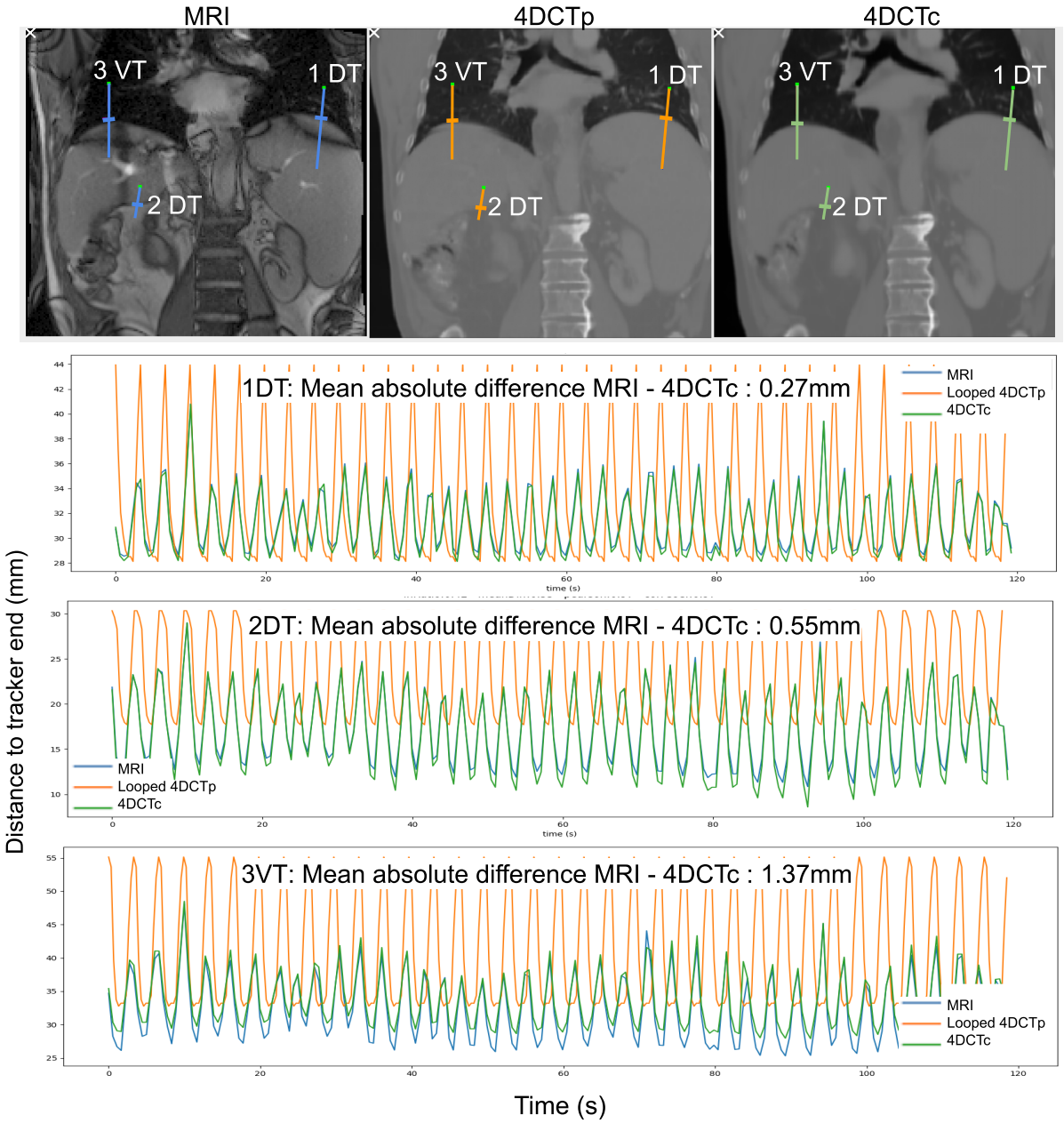


Figure 6. Example of motion tracked by three trackers. The motion is tracked in the tracker direction and given as the distance between the detected border and the tracker extremity (green dot). The difference between the MRI and the generated 4DCTc is computed for two driving trackers (1 DT and 2 DT) and one representative validation tracker (3 VT). The looped 4DCTp signal is also shown to show the baseline shift between the first tracker, where the MRI is always inside the 4DCTp range, and the other two, where the MRI signals are outside the 4DCTp range about half the time.

## 3. Results

All tracker results for all patients are shown in Figure 7. The average absolute difference between the reproduced motion and the MRI sequence is 0.93 mm (std: 0.66 mm) for DT's (84 trackers) and 1.7 mm (std: 1.14 mm) for VT's (92 trackers). This is a significant improvement over our previous work [11] without the weight maps and local tuning, which reported a mean difference of 1.64 mm (std=0.91)

for DT's and 2.2 mm (std=1.18) for VT's (24 trackers each). Likewise, the improvement in the tissue border positions reproduced by the model can be represented by the difference between these two average values: 1.64 mm - 0.93 mm = 0.71 mm for areas selected to drive the model and 2.2 mm – 1.7 mm = 0.5 mm for validation areas. We compared the distributions of the tracker results with and without the additional step to adjust locally the deformation fields with T-tests and got a p-value under 0.05 for both DT's and VT's cases, showing that the improvement in accuracy is significant.

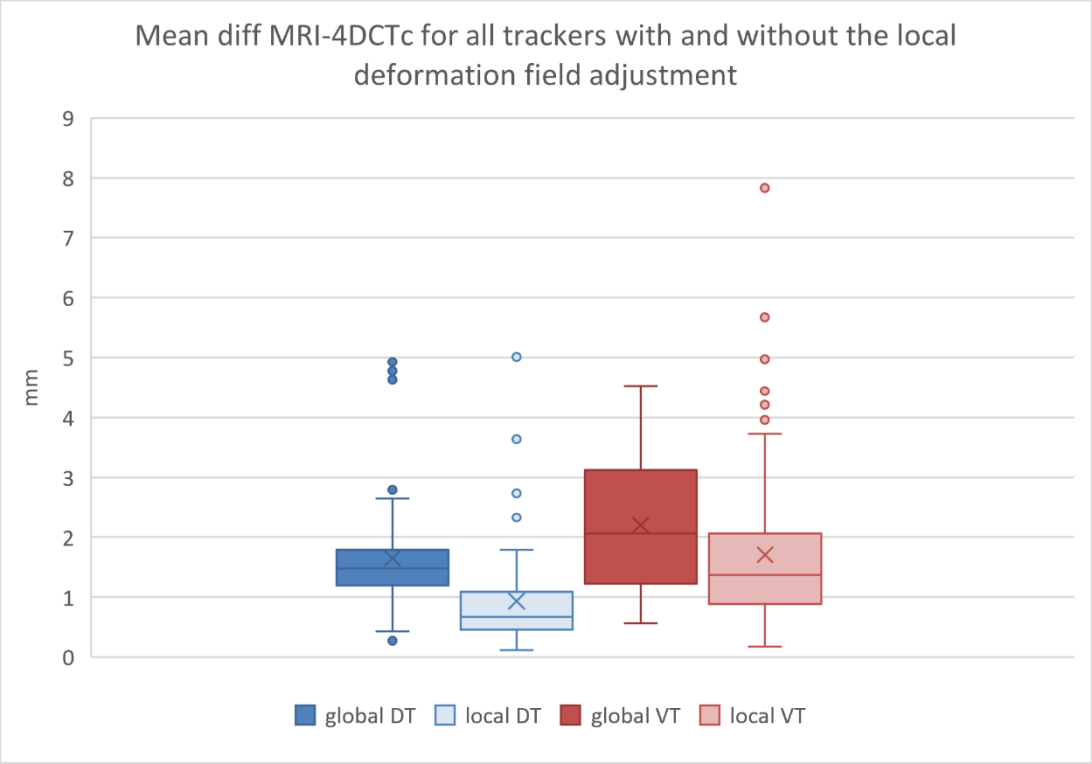


Figure 7. Box plot of all tracker results, split into Driving Trackers (DT in blue) and Validation Trackers (VT in red), with (local) and without (global) the local tuning of the deformation fields. The average value (crosses) is 1.64 (std=0.91) and 0.93 mm (std=0.66) for 53 global and 81 local DT's respectively, and 2.2 (std=1.18) and 1.7 mm (std= 1.14) for 53 global and 92 local VT's respectively. The box is the standard 25%-75% interquartile range (IQR) and points are outliers if 1.5 times the IQR above the third quartile or under the first quartile.

As the deformation field is adjusted locally and systematic differences can occur between the 4DCTp and the cine-MRI acquisition that may take place several days later, we suppose that the distance from the driving trackers has an impact on the reproduced positions and motion. To verify this, we plotted the validation trackers results in function of their distance from the closest driving trackers [Figure 8]. As expected, we found the tissue border positions in the 4DCTc to be closer to the ground truth for VT's closer to DT's, confirming the importance of selecting areas to drive the model principally in the beam path and around the target.

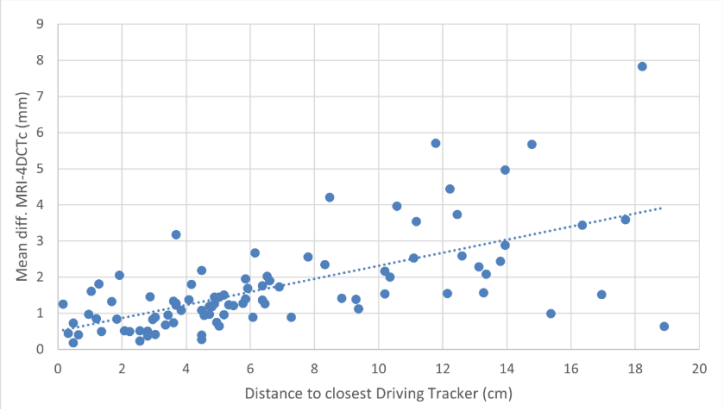


Figure 8: Scatter plot of the absolute value of the mean difference between the tracked border positions on the MRI and the 4DCTc for 92 Validation Trackers in function of the distance with the closest Driving Tracker. The dotted line is the linear regression line that confirms the expected trend.

In creating all the 4DCTc images, we also saved the value of the 3D deformation applied to the tumor center. We analyzed the correlation between the motion of the tumor and the trackers grouped by anatomical region (hepatic dome, left diaphragmatic dome, visceral liver surface, right kidney, skin, etc.). Except for the skin, which gave worse correlations, as expected [18], we did not find significant differences in correlations between anatomical areas to give guidelines for the ideal tracker positions [Table 1].

| | Hepatic dome | Left diaphragmatic dome | Visceral liver surface | Right kidney | Skin |
|---|---|---|---|---|---|
| Average cross-correlation | 0.71 | 0.71 | 0.76 | 0.68 | 0.54 |

Table 1. Average cross-correlations between the motion of the tumor in the 4DCTc and the motion of trackers in the MRI by anatomical site.

The coronal and sagittal slices are used independently, each slice giving another 3DCT for the 4DCTc. But as they come from the same coronal-sagittal interleaved acquisition, it is possible to compare the results of the method on both series to detect a baseline shift in one direction and not the other, for example due to a small rotation. For six of the thirteen patients in whom the tumor and the coronal and sagittal planes were not too close to the border of the liver, we were able to place trackers on the hepatic dome on either side of the sagittal and coronal planes' intersection. For those patients, we extracted the 3D motion of the tumor during the 4DCTc sequence's creation and compared the motion coming from the subsets of 3DCT images created using only the coronal slices and only the sagittal slices, respectively. The example in Figure 9 shows that both motions are well matched. If it is not the case, this can be a way to detect a baseline shift such as small rotations around a specific axis between the 4DCTp and the MRI.

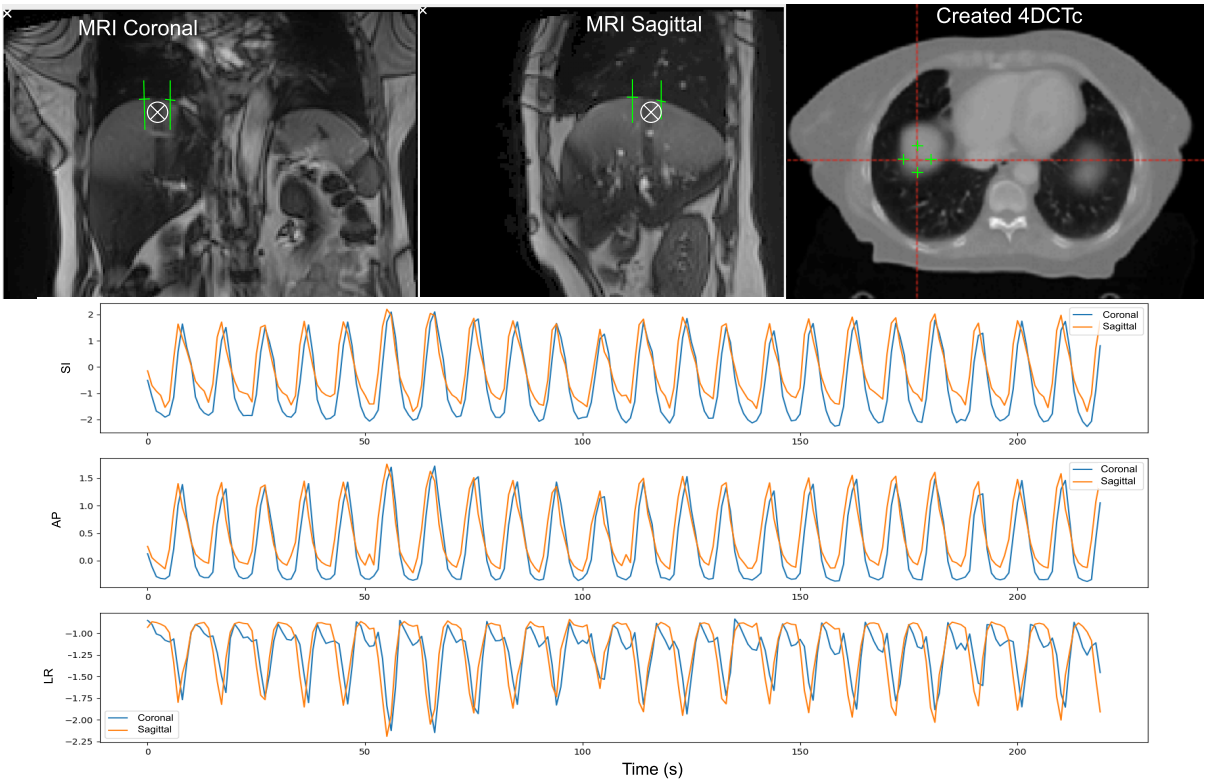


Figure 9. 3D motion of the tumor center (white X) extracted from the created 4DCTc sequence and compared for images created using the coronal (blue signal) and sagittal (orange signal) slices separately. The motion is shown in the three standard directions, Superior-Inferior (SI), Anterior-Posterior (AP) and Left-Right (LR). The 4DCTc from which the motion is extracted is created using the green trackers placed on either side of the other plane, as shown on the MRI slices (top left and center) and the transverse CT slice (top right).

We also tried to quantify the effect of breathing outside the range of the original 4DCTp on the accuracy of the reproduced motion (example in Figure 6), since extrapolation can multiply small errors by the extrapolation factor $r_k > 1$. We computed the correlation coefficient between the percentage of the MRI border position outside the range of the planning 4DCTp phases and the precision of the reproduced motion in the 4DCTc (mean absolute difference MRI-4DCTc), but no significant correlation was found (Pearson coefficient of -0.16).

Multiplying the fields $DT_k$ by their respective weight maps $W_k$ and adding them to the final field $DF_i$ for an image of 340 x 360 x 60 voxels takes around 40 ms for each tracker with our unoptimized code on a decent laptop (2.9 GHz Intel Core i7 7820HQ). The computation time scales linearly with the size of the area to deform.

## 4. Discussion

The difference between the tracked border positions in the 4DCTc and in the cine-MRI is measured for multiple areas, but all in the same slice, which is the only ground truth available during treatment. Given the results in function of the distance to driving trackers [Figure 8] and the nature of the method, we suppose that the farther we go from the MRI slice position, the less likely our deformed image is to match the patient's real anatomy exactly, because the distance from the driving trackers increases. We think using the VT set is enough to validate the method in and close to the MRI slice; we see no reason why the method would behave differently outside the MRI plane. If the validation

trackers give a low difference even for trackers placed in the slice but far from driving trackers (more than 20 cm away, for example), that indicates that there are not a lot of non-breathing-related changes between the 4DCTp and the cine-MRI image acquisitions. That is a good indication that the deformation in the third dimension should also behave well, at least close to the MRI slice. Now, if a larger tissue border position difference is measured by a VT, that signals that either non-breathing-related anatomical changes have occurred between the model source images and the cine-MRI (a baseline shift) or the breathing pattern deviates greatly from what is contained in the 4DCTp (a big extrapolated case, for example). The advantage of the fast border tracking method is that it can give this feedback in real-time during treatment.

Full 3D validation using validation trackers outside the MRI slice plane would have allowed us to verify this hypothesis but, unfortunately, it was not possible to acquire 4D MRI data retrospectively for our patients. Given that our application targets radiotherapy, reproducing an image far from the beam correctly is not really important and using such a 3D validation would be useful mainly to detect whether the 4DCTp was out of date. The important part of the image is the beam path, and we think a small set of 2D slices is enough to capture what happens in this area precisely without the need for a 3D ground truth. The possibility of linking the treatment to acquisition allows the two to be synchronized in such a way that the chosen slice position is always where the beam is currently irradiating the patient. Interleaved planes such as we have for the patients of this study, or multiple slices in the same plane, while not technically a 3D validation, are used to validate the accuracy of the transferred motion for different planes successively, several times each second.

It is possible to reproduce a baseline shift occurring between the motion model's creation and its online application, and it is also possible to reproduce a different breathing pattern from what is already in the 4DCTp (for example, if the breathing changes from chest to abdominal breathing). Nevertheless, both of these irregular sources of motion or a combination of the two are more difficult to represent with this model because the result will depend on whether trackers can be placed in these areas. To avoid this, we still recommend updating the 4D image and motion model as regularly as possible. This can now be done using 4DMRI to reduce the imaging dose given during the treatment period [19], or with a deep learning method to create a 4DCT using only one 3DCT [20]. Note that this is valid for any model we could use instead of the fast border tracking method we tried here. Whatever the method, updating the 4D image set right before the application is ideal. The same can be said for the cine-MRI to 4DCTp registration we use in the preparation step. Checking regularly if the images are still aligned is of course always better. One good option would be to re-do the registration when there are pauses in the treatment like in between 2 beam positions.
We prefer to use our model with a 4DCT over a 4DMRI because this way the result is of CT modality. The treatment delivery can then be simulated on the 4DCTc sequence to accumulate the dose considering the real breathing pattern of the patient during the 2 minutes of the cine-MRI acquisition. It could also be used with a 4DMRI if the goal is simply to check the anatomy in real-time.

While this method does add a step to existing methods relying on precomputed deformation fields, the added computation time can be quite brief, depending on the size of the image to deform and the number of different deformation fields to sum. We measured an additional time of 40 ms/area on top of the time necessary for our previous method for a 340 x 360 x 60-voxel volume, which is a realistic volume for a radio- or proton therapy beam path. This time must be added to the time necessary to use the chosen 2D to 3D motion model (with our model on laptop, it was between 40 and 320 ms depending on the number of trackers and the size of the area to deform). This is important to consider if the goal is to apply the method online. The real-time constraints will depend on the objective of the application and on the other timings involved, such as the image acquisition time and the different hardware response timings. We don't know yet what will be the best online use for such a method. It could be used to verify if the anatomy is still in acceptable boundaries to deliver the

treatment, to accumulate the delivered dose with a small delay during the treatment, or to guide a 4D treatment based on multiple scenarios like a multi-gating method. If the method is too slow to make a decision on the treatment based on the last acquired frame, it could maybe be used with a motion prediction tool to create an estimated 3D image of a couple of seconds in the future and increase the time available to make a decision. The ultimate goal would be to track and aim at the tumor continuously, which is difficult in proton because the entire 3D image and computing a dose estimation is necessary in real-time.

While the border tracking method we used to test our new deformation field combination method is the fastest so far, has similar performances to the other methods [21], and gives immediate feedback on the results, it relies on the use of manually placed trackers, which is not ideal if it is to become a clinical solution. Increasing the speed of an automatic solution or combining the advantages of several options would be better and more realistic to approach a real-time guiding solution. AI might be a good approach to automate modern treatment steps [22].

## 5. Conclusion

Using this method on top of existing methods to drive 3D motion models based on precomputed deformation fields improves the accuracy of the reproduced motion. Our method does add some computation time, which could be an issue in the case of real-time use, depending on the size of the area to deform.

References


[1] Lin, L., Souris, K., Kang, M., Glick, A., Lin, H., Huang, S et al. Evaluation of motion mitigation using abdominal compression in the clinical implementation of pencil beam scanning proton therapy of liver tumors. Medical physics. 2017. 44(2), 703-712. **https://doi.org/10.1002/mp.12040**

[2] Van Ooteghem G, Dasnoy-Sumell D, Lambrecht M, Reychler G, Liistro G, Sterpin E et al. Mechanically-assisted non-invasive ventilation: a step forward to modulate and to improve the reproducibility of breathing-related motion in radiation therapy. Radiotherapy and Oncology. 2019 Apr 1;133:132-9. https://doi.org/10.1016/j.radonc.2018.12.026

[3] Knopf AC, Boye D, Lomax A, Mori S. Adequate margin definition for scanned particle therapy in the incidence of intrafractional motion. Physics in Medicine & Biology. 2013 Aug 13;58(17):6079. https://doi.org/10.1088/0031-9155/58/17/6079

[4] Buti G, Souris K, Montero AM, Lee JA, Sterpin E. Towards fast and robust 4D optimization for moving tumors with scanned proton therapy. Medical physics. 2019 Dec;46(12):5434-43. https://doi.org/10.1002/mp.13850

[5] Czerska K, Emert F, Kopec R, Langen K, McClelland JR, Meijers A et al. Clinical practice vs. state-of-the-art research and future visions: Report on the 4D treatment planning workshop for particle therapy–Edition 2018 and 2019. Physica Medica. 2021 Feb 1;82:54-63. https://doi.org/10.1016/j.ejmp.2020.12.013

[6] Chin S, Eccles CL, McWilliam A, Chuter R, Walker E, Whitehurst P et al. Magnetic resonance-guided radiation therapy: a review. Journal of medical imaging and radiation oncology. 2020 Feb;64(1):163-77. https://doi.org/10.1111/1754-9485.12968

[7] Paganelli C, Portoso S, Garau N, Meschini G, Via R, Buizza G et al. Time-resolved volumetric MRI in MRI-guided radiotherapy: an in silico comparative analysis. Physics in Medicine & Biology. 2019 Sep 19;64(18):185013. https://doi.org/10.1088/1361-6560/ab33e5

[8] Stemkens B, Tijssen RH, De Senneville BD, Lagendijk JJ, Van Den Berg CA. Image-driven, model-based 3D abdominal motion estimation for MR-guided radiotherapy. Physics in Medicine & Biology. 2016 Jun 30;61(14):5335. https://doi.org/10.1088/0031-9155/61/14/5335

[9] Harris W, Ren L, Cai J, Zhang Y, Chang Z, Yin FF. A technique for generating volumetric cine-magnetic resonance imaging. International Journal of Radiation Oncology* Biology* Physics. 2016 Jun 1;95(2):844-53. https://doi.org/10.1016/j.ijrobp.2016.02.011

[10] Fayad HJ, Buerger C, Tsoumpas C, Cheze-Le-Rest C, Visvikis D. A generic respiratory motion model based on 4D MRI imaging and 2D image navigators. In2012 IEEE nuclear science symposium and medical imaging conference record (NSS/MIC) 2012 Oct (pp. 4058-4061). IEEE. https://doi.org/10.1109/NSSMIC.2012.6551927

[11] Seregni M, Paganelli C, Kipritidis J, Baroni G, Riboldi M. Out-of-plane motion correction in orthogonal cine-MRI registration. Radiother Oncol. 2017 May 1;123:S147-8. https://doi.org/10.1016/s0167-8140(17)30725-9

[12] Dasnoy-Sumell D, Souris K, Van Ooteghem G, Macq B. Continuous real time 3D motion reproduction using dynamic MRI and precomputed 4DCT deformation fields. Journal of Applied Clinical Medical Physics. 2020 Aug;21(8):236-48. https://doi.org/10.1002/acm2.12953

[13] Garau N, Via R, Meschini G, Lee D, Keall P, Riboldi M, Baroni G, Paganelli C. A ROI-based global motion model established on 4DCT and 2D cine-MRI data for MRI-guidance in radiation therapy. Physics in Medicine & Biology. 2019 Feb 5;64(4):045002. https://doi.org/10.1088/1361-6560/aafcec

[14] Janssens G, Jacques L, Orban de Xivry J, Geets X, Macq B. Diffeomorphic registration of images with variable contrast enhancement. International journal of biomedical imaging. 2011 Jan 1;2011. https://doi.org/10.1155/2011/891585

[15] Wolthaus JW, Sonke JJ, Van Herk M, Damen EM. Reconstruction of a time-averaged midposition CT scan for radiotherapy planning of lung cancer patients using deformable registration a. Medical physics. 2008 Sep;35(9):3998-4011. https://doi.org/10.1118/1.2966347

[16] Duerk JL, Lewin JS, Wendt M, Petersilge C. Remember true FISP? A high SNR, near 1-second imaging method for T2-like contrast in interventional MRI at. 2 T. Journal of Magnetic Resonance Imaging. 1998 Jan;8(1):203-8. https://doi.org/10.1002/jmri.1880080134

[17] Liang Z, Liu H, Xue J, Hu B, Zhu B, Li Q et al. Evaluation of the intra-and interfractional tumor motion and variability by fiducial-based real-time tracking in liver stereotactic body radiation therapy. Journal of applied clinical medical physics. 2018 May;19(3):94-100. https://doi.org/10.1002/acm2.12292

[18] Paganelli C, Seregni M, Fattori G, Summers P, Bellomi M, Baroni G et al. Magnetic resonance imaging–guided versus surrogate-based motion tracking in liver radiation therapy: a prospective comparative study. International Journal of Radiation Oncology* Biology* Physics. 2015 Mar 15;91(4):840-8. https://doi.org/10.1016/j.ijrobp.2014.12.013

[19] Boye D, Lomax T, Knopf A. Mapping motion from 4D-MRI to 3D-CT for use in 4D dose calculations: A technical feasibility study. Medical physics. 2013 Jun;40(6Part1):061702. https://doi.org/10.1118/1.4801914

[20] Mori S, Hirai R, Sakata Y. Simulated four-dimensional CT for markerless tumor tracking using a deep learning network with multi-task learning. Physica Medica. 2020 Dec 1;80:151-8. https://doi.org/10.1016/j.ejmp.2020.10.023

[21] Paganelli C, Portoso S, Garau N, Meschini G, Via R, Buizza G, Keall P, Riboldi M, Baroni G. Time-resolved volumetric MRI in MRI-guided radiotherapy: an in silico comparative analysis. Physics in Medicine & Biology. 2019 Sep 19;64(18):185013. https://doi.org/10.1088/1361-6560/ab33e5

[22] Cusumano D, Boldrini L, Dhont J, Fiorino C, Green O, Güngör G et al. Artificial Intelligence in magnetic Resonance guided Radiotherapy: Medical and physical considerations on state of art and future perspectives. Physica Medica. 2021 May 1;85:175-91. https://doi.org/10.1016/j.ejmp.2021.05.010